 doi:10.20944/preprints202203.0392.v1

Article

Simulation-based process design for the asymmetric single point incremental forming of individual hip cup prosthesis made of titanium alloy

Sirine FRIKHA [1,2]*, Laurence GIRAUD-MOREAU [1], Anas BOUGUECHA [2] and Mohamed HADDAR [2]

[1] Life Assesment of Structures, Materials, Mechanics and Integrated Systems (LASMIS), University of Technology of Troyes, 12 Rue Marie Curie, 10004 Troyes, France; sirine.frikha@utt.fr; laurence.moreau@utt.fr;
[2] Laboratory of Mechanics, Modeling and Production (LA2MP), National Engineers School of Sfax, Route de Soukra, 3038 Sfax, Tunisie; anas.bouguecha@gmx.de; mohamed.haddar@enis.tn
* Correspondence:sirine.frikha@utt.fr

Abstract: Advanced manufacturing techniques, aimed at implants with high dependability, flexibility, and low manufacturing costs, are crucial in meeting the growing demand for high-quality products like biomedical implants. Incremental sheet forming is a promising flexible manufacturing approach for rapidly prototyping sheet metal components using low-cost tools. Titanium and its alloys are used to shape most biomedical implants because of its superior mechanical qualities, biocompatibility, low weight, and great structural strength. The poor formability of titanium sheets at room temperature, however, limits their widespread use. The goal of this research is to show that gradual sheet formation of a titanium biomedical implant is possible. The possibility of creative and cost-effective concepts for the manufacturing of such complicated shapes with significant wall angles is explored in this study. A numerical simulation based on finite element modeling as well as a design process tailored to metal forming is used to complete the development. The mean of uniaxial tensile tests with a constant strain rate was used to study the flow behavior of the studied material. To forecast the crack, the obtained flow behavior was modeled using the behavior model and failure model.

Keywords: Incremental Forming; Finite Element simulation; biomedical implants; titanium; wall angle

1. Introduction

Total Hip Arthroplasty (THA) is an intervention in order to restore mobility and relieve chronic pain in people with certain pathologies such as osteoarthritis. It is defined as a surgical intervention that involves replacing the potentially damaged neck and head of the femur (cf. Figure 1) with prosthetic components that represent a metal alloy implant. This intervention involves several stages. First, the damaged femoral head is removed and replaced with a metal rod which is placed in the hollow center of the femur. The femoral stem can either be cemented or "pressed" into the bone. Then a metal or ceramic ball is placed on the top of the stem replacing the damaged femoral head that has been removed. As a result, the damaged cartilaginous surface of the socket (acetabulum) is removed and replaced with a metal socket. Screws or cement are sometimes used to hold the socket in place. Finally, a plastic, ceramic or metal spacer is inserted between the new ball and the socket to allow a smooth sliding surface.

Patients with osteoarthritis, dysplasia, malignancies, hip necrosis, or congenital hip morphologic anomalies are typically treated with THA. Indeed, arthritis is the leading cause of THA, with osteoarthritis, rheumatoid arthritis, and traumatic arthritis being the most prevalent types.

 doi:10.20944/preprints202203.0392.v1

(a) Before Total Hip Arthroplasty

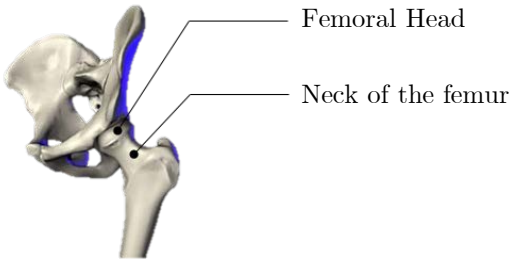

(b) After Total Hip Arthroplasty

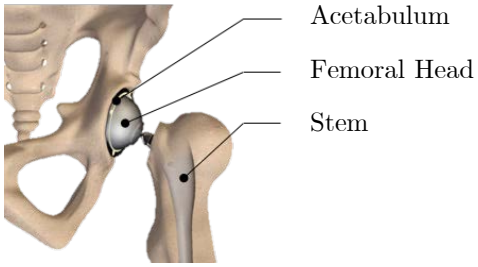

Figure 1. Pelvic bone

More than 600,000 hip procedures are performed each year in Europe [1], with more than 183,000 in France [2], 280,000 in the United States [3], and 1.4 million globally. By 2030, these statistics are likely to skyrocket [4–7]. According to the world's leading market research shop, the number of primary total hip replacements has increased in this era because to the ongoing COVID-19 pandemic [8] (RESEARCHANDMARKETS).

In general, the method for manufacturing a total hip arthroplasty is heavily influenced by the materials to be used for each component. Investment casting or forging are used to create materials like cobalt chrome, stainless steel, and titanium, which are then rough machined, polished, and coated. Molding and machining are required for materials such as ultra-high molecular weight polyethylene. Sintering, followed by grinding, polishing, and lapping, is how ceramic biomaterials elements like alumina and zirconia femoral balls are made. Ref. [9–11] for more information. Because shape correctness, prosthetic surface integrity, and surface roughness all play a part in their longevity. Because polishing is the most common method of achieving these results. To ensure high engagement stability when a patient engages in various types of exercise and motion, the acetabular socket and bearing surfaces of the femoral ball must have a high grade of surface polish.

Hip cups are traditionally made by CNC machining from bar stock, and up to 80% of the material used in prosthesis implant fabrication is lost, according to [12]. In terms of flexibility, cost, and rapid prototyping, additive manufacturing (AM) [13] and incremental sheet forming (ISF) are today's alternative manufacturing processes. Another RM technique, electron beam melting (EBM), has shown promise in the fabrication of custom orthopedic hip stems with tailored material properties in a study by Harrysson et al.[14], generating open-celled titanium components by Heinl et al.[15], and manufacturing acetabular cups with integrated surface structures by Thundal et al.[16], to name a few. [17] by Syam et al. provides a summary of recent developments in the field of AM for medical applications.

Cronskär et al.[18] conducted comparison research between traditional machining and AM using electron beam melting (EBM). By conducting a practical investigation, the practicality and commercial potential of employing EBM for the fabrication of hip implants is compared to using conventional machining in terms of material consumption, associated expenses, and manufacturing time. Implants are traditionally made in a

 doi:10.20944/preprints202203.0392.v1

machine tool shop throughout numerous operations. Milling and sculpture are done using a multi-operational lathe. A turning operation is then used to manufacture the cone component. Finally, to meet the requirement for high surface smoothness in certain regions, manual grinding and polishing are required. The cost of EBM-based manufacturing was 35 percent less than the cost of conventional manufacturing, according to the cost comparison.

However, we must be mindful of the restrictions that result in flaws in the built part, as well as the dangers of defects specific to the AM method. The inclusion of holes or pores in the final part's structure, which might alter its mechanical qualities, is one of the most common limitations.[19] These flaws might be caused by the powder feedstock's characteristics or by poor construction conditions. If the powder is not entirely melted, spherical gas pores can be transmitted to the finished item; similarly, gasses from the build chamber can be caught in the melt pool throughout the process, resulting in spherical voids [20].

Another source of faults is in the so-called "keyhole melting" mode, in which the depth of the melt pool is controlled by the metal evaporation caused by the high-power energy source. When the vapor cavity collapses, approximately spherical voids remain [21]. If there is a lack of fusion between consecutive layers, elongated voids can be created (lack of fusion defects). Another common limitation is the presence of solid powder particles partially attached to the built part's surface; if the energy source is too low, the powder is not completely molten, whereas if it is too high, the molten pool can form small 'islands' that generate particles ('balling phenomenon') [19].

Cracking and delamination are two other possible faults in 3D printed items; these can occur as a result of the structure's solidification shrinkage (thermal contraction), which causes tensile stresses that form cracks at the grain boundaries if the material's strength is exceeded. When residual pressures at the interface of the following layers exceed the metal's strength, a delamination phenomenon of these successive layers can occur [19]. A condition known as alloying element loss can occur when the melting material's temperature is too high.

As seen in Figure 1, the femoral ball that inserts inside the socket allows the hip joint to articulate like a mechanical bearing. The following properties are required of materials for hip joint prostheses: (a) high biocompatibility with tissues and bones; (b) sufficient mechanical strength, e.g., suitable Young's modulus, fracture toughness, and fatigue life; (c) low friction but high wear resistance; and (d) chemical stability and safety. The materials utilized and the head diameter affect the wear of hip joint prostheses.

A larger femoral ball, for example, wears faster in a metal-on-polyethylene-bearing combination, even though thethe fact that a larger head increases range of motion and minimizes dislocation. From a manufacturing standpoint, the bearing surfaces of the femoral ball and acetabular socket must have critical that the bearing surfaces of the femoral ball and acetabular socket have a high level of surface quality and maintain good bearing engagement stability while a patient moves in various ways. Only a well-designed fabrication technology can achieve these.

Aside from the manufacturing process, the lifespan of a conventional prosthesis is a significant consideration. Although the THA prosthesis has a 10-year lifespan, there are significant hazards associated with the treatment. For starters, blood clots in the legs' veins can form after surgery, which can be harmful if they break off and move to the lungs, heart, or, in rare cases, the brain. Infection can then develop at the incision site as well as in the deeper tissues around the new hip. Antibiotics are used to treat most infections, but a significant infection around the prosthesis may necessitate surgery to remove and replace it. Another danger is that the legs' length will alter. Despite the surgeon's best efforts, a new hip may cause one leg to be longer or shorter than the other. Contracture of the muscles around the hip can sometimes cause this.

Dislocation is also a possibility because certain positions might cause the ball to come out of the new joint in the socket, particularly in the first few months after surgery,

 doi:10.20944/preprints202203.0392.v1

necessitating surgery to stabilize it. Loosening can also occur with fresh implants, even though the fact that this is a rare problem. Because the new joint may not adhere securely to the bone or loosen over time, causing hip pain and necessitating surgery to correct the problem, this is the case. Finally, there is a possibility that a hip migration occurs as a result of the bone alteration [22–24]. During the implantation of traditional hip prostheses, the surgeon performs a substantial bone resection to ensure the precise location of the cup in the pelvis bone for a sufficiently stable anchoring of the prosthesis. The danger of dislocation described in the previous paragraph is increased by this technique.

It can be prevented, though, by creating a custom-made cup that is specifically fitted for the patient undergoing surgery. Indeed, because the cup is directly created to match perfectly with the shape of the affected patient's pelvic bone, individualization of the hip cup is regarded as an excellent method for reducing the amount of bone tissue removed during the procedure. Furthermore, when aesthetic compatibility is desired, bespoke implants are the gold standard. It also improves the implant's anchoring, which lowers the cup's migration [25–27].

Individual prostheses are typically created using a reverse engineering process to fit the patient. Behrens et al. [28,29] established a method for producing these hip prosthesis cups using traditional sheet metal forming procedures including stamping and hydroforming. Individualization of the cup in this scenario necessitates the creation of customized equipment such as the die and punch that is unique to each patient. As a result, mass production becomes more sophisticated, resulting in higher production costs.

Individualization of made-to-measure cups is often reserved for cases of malignancies of the hip joint or the treatment of significant abnormalities due to the high expense involved with this sort of manufacturing procedure in the case of made-to-measure cups. To generalize cup individualization and so profit from its benefits while restricting economic constraints, it is required to employ a flexible technique that allows different cup portions to be manufactured without incurring relatively large additional expenses.

ISF (incremental sheet forming) is an excellent forming technique. The ISF methods have several advantages, including no waste of raw material, improved product mechanical qualities, and a faster production rate. ISF is used in big batches to amortize tooling expenses and produce large quantities of components in a short period of time. Traditional stamping procedures, on the other hand, are prohibitively expensive for small numbers or bespoke prototypes. ISF technology offers a novel way to reduce the cost of solving the problem in small-scale production. It introduces the cost-effective use of metallic sheets for small-batch manufacture without the use of expensive or specialized machines.

It's not easy to find the right material and manufacturing technique to create a personalized implant with optimal biomechanical qualities. The literature contains a wealth of information on the use of a variety of biomaterials, ranging from metals to bioceramics and biopolymers, but titanium (Ti) and its alloys remain the most widely used solutions because they have a low Young's modulus (ensuring a uniform stress distribution between the implant and the surrounding bone), excellent mechanical properties, and, in terms of biocompatibility, the ability to promote osseointegration.

2. Related work

We give a quick overview of the ISF (cf. Figure 2) in this section. Recent bioengineering and manufacturing research has revealed a growing demand for high-quality final products, particularly biomedical implants capable of extending patients' lives while avoiding protracted hospitalization [30].

Over the last decade, incremental sheet forming (ISF) has been the topic of extensive research. Many enhancements to the process capabilities and the forming mechanism have resulted since Leszak's original design was filed as a patent in 1967 [31]. Jeswiet et

 doi:10.20944/preprints202203.0392.v1

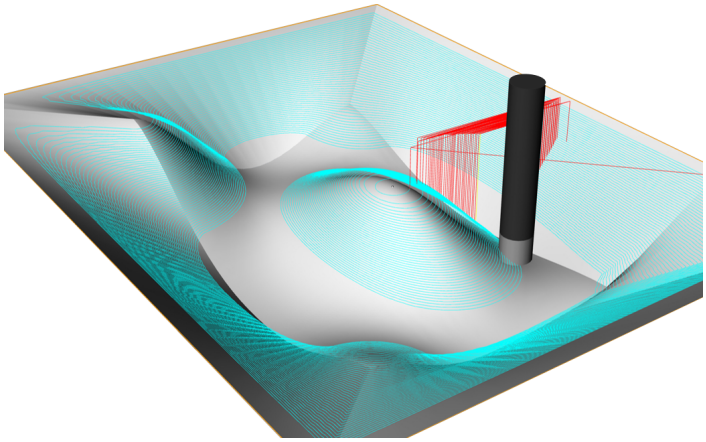

Figure 2. Incremental forming process

al. study [32] laid the groundwork for key developments in Incremental Sheet Forming at the time, while Emmens et al. [33] provided an update on future developments. Since then, there has been a considerable increase in the number of studies concentrating on ISF.

Furthermore, the Single Point Incremental Forming (SPIF) technology [34] has made its way into the manufacturing sector as a growing alternative for small batch production, quick prototyping, and bespoke products and complex parts. The ISF is a low-cost forming technique due to the machine's flexibility[35]. The cost savings come from the elimination of traditional instruments like the die and punch. The SPIF is characterized by clamping the sheet on all of its edges and applying repeated forces in the form of a controlled movement that forms the required geometry via the imposed action of a local strain on the metal sheet[36]. A hemispherical punch deforms the sheet.

Severe plastic deformation causes grain refinement and an increase in the high angle grain boundary, both of which are helpful to subsequent plastic forming [37]. Several experiment and analytic methods were used to determine the impact of shaping parameters. Saidi et al. [38–40] carried out a series of Taguchi method experiments, and the results showed that the thickness of the sheet, the step-down size, and the wall angle all have a significant effect on the forming process, which can be used as a guideline for future research. In their work, Saidi et al. demonstrated that manufacturing direct parts with a wall angle greater than 40° at ambient temperature is unfeasible.

Although there is a wealth of information on the use of a variety of biomaterials, ranging from metals to bioceramics and biopolymers, titanium (Ti) and its alloys remain the most widely used solutions because they have a low Young's modulus (ensuring uniform stress distribution between the implant and the surrounding bone), excellent mechanical properties, and the ability to promote osseointegration in terms of biocompatibility.

Few studies have focused on multi-pass solutions for reducing failure, attaining a rigid body transition, and increasing strain throughout the wall. Generally, improving the thickness of the risk zone is emphasized in to enhance the wall angle limit. Behera et al. [41] divided improving the wall angle limit into three categories: I multistep toolpath tactics, (ii) workpiece orientation, and (iii) thermal procedures using lasers, electricity, and other means. A high wall angle targeted shape is accomplished using a classic multi-step technique by sequentially generating numerous intermediate shapes numerous intermediate shapes sequential manner. For axisymmetric components, Kitazawa and Nakajima [42] used multi-step formation procedures.

For non-axisymmetric pieces, Hirt et al. [43] devised a modified multi-step forming technique. Shamwari et al. [44] integrated a bulging approach with SPIF to fully use the material's deformation potential in the blank's undeveloped middle section. Although

Preprints (www.preprints.org) | NOT PEER-REVIEWED | Posted: 30 March 2022 doi:10.20944/preprints202203.0392.v1

this procedure improved the formability of a truncated cone, it did result in a bulge at the bottom of the produced object.

Furthermore, a comparison of the generated shape profile between simulation and experiment revealed a significant variation, particularly towards the bottom of the workpiece. A consistent strain distribution, on the other hand, prevents cracking and allows for the formation of a high wall angle shape. By combining In-to-Out(I/O) and Out-to-In(O/I) toolpaths for each intermediate form, Malhotra et al. [45] devised a new toolpath technique to achieve a smoother component. There has never been a quantitative method for designing an ideal multistep strategy or establishing a relationship between the tool radius and its vertical displacement in each step.

The goal of this research was to develop a titanium hip cup prosthesis with a complex shape (asymmetric shape) and a wall angle. We present a new method for obtaining a healthy component that combines the incremental forming process with deep drawing to achieve this goal. Simulations including the containment features of biomedical designs could be performed using a verified Johnson-Cook model. The factors that can be utilized to forecast failure in commercially pure Grade 2 α-titanium are determined and evaluated in this study. The titanium parameters used in this investigation were derived through simulation tensile tests that were carefully optimized.

3. Materials and Methods

3.1. Material and experimental characterisation

The material used in this study is Grade 2 α-titanium, which is commercially pure. Table 1 shows the chemical composition of the tested material, which is compared to the **ASTM** standard composition (in weight percent) for this material. The titanium was purchased in the form of a 1 mm thin plate, which was subsequently sliced into samples using the ISO 6892-1 water jet cutting procedure. Specimens are made from material in the rolling (RD), normal (ND), and transverse (TD) directions, as illustrated in Figure 3. Tensile tests were performed on these specimens using an **Instron® 4411** type testing equipment with a 5 kN capacity, as illustrated in Figure 4, at room temperature with a cross head speed of 1 mm/min to gather flow stress-strain data to analyze the deformation flow behavior.

The study's second batch of samples was used to look into the impact of stress triaxiality, mechanical behavior, and Johnson-Cook damage parameters. Smooth and notched samples were both subjected to tensile tests. Technical drawings of smooth and notched tensile test specimens are shown in Figure 5. The notch radius of the notched specimens is represented by R_0. For the processing of specimens, three different notch radiuses were used. The specimens' radiuses and gauge lengths are reported in Table 2.

To ensure uniformity of results, each uniaxial monotonic tensile test was repeated four times for each case during the experiment. As a result, four repetitions for each of the six specimens were carried out, totaling 24 tensile tests. All of the trials were carried out in accordance with the ISO standard.

A non-destructive image correlation technique was utilized to evaluate the deformations of a sample, which is based on the analysis of photos captured during mechanical testing. Digital cameras with high-resolution capture a sequence of photos that track the distortion over time. The LAVISION® software then interprets the images. The employment of two cameras (stereoscopic vision) allows for the measurement of deformation fields in three dimensions. The force was measured using a load cell, and the stress was calculated using the following standard strength equation:

$$\sigma = \frac{F}{A_0} \tag{1}$$

$$\epsilon_{\text{eng}} = \frac{\Delta \ell}{\ell_0} \tag{2}$$

Preprints (www.preprints.org) | NOT PEER-REVIEWED | Posted: 30 March 2022 doi:10.20944/preprints202203.0392.v1

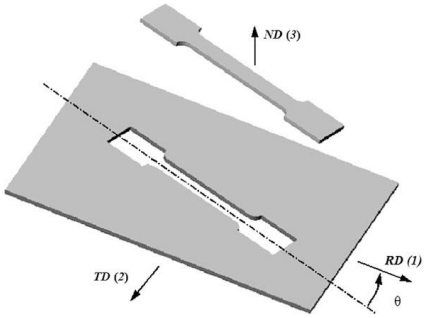

Figure 3. Representation of three directions [46]

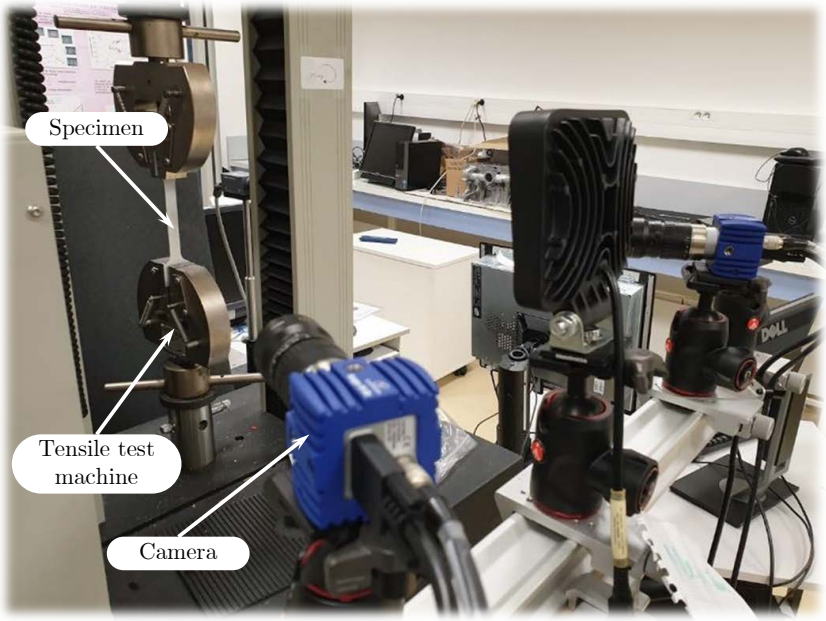

Figure 4. Experimental Setup

$$\begin{aligned} \sigma_{\text{true}} &= \sigma_{\text{eng}}(1+\epsilon_{\text{eng}}); \\ \epsilon_{\text{true}} &= \ln(1+\epsilon_{\text{eng}}), \end{aligned} \tag{3}$$

where σ is the Stress (in MPa), F the force (in N), A_0 the section (in mm^2), ϵ_{eng} the engineer strain (unitless), $\Delta\ell$ the displacement (in mm), ℓ_0 the initial length (in mm), σ_{true} is the real stress (in MPa), σ_{eng} the engineer stress (in MPa) and ϵ_{true} the real strain (unitless).

Table 1. Comparison of the **ASTM** standard and the chemical composition of Grade 2 α-titanium.

Chemical composition (Wt.%)	Used Sample	ASTM F67
Titanium	49.7 %	32.5 %
Iron	20 %	30 %
Oxygen	18 %	25 %
Carbon	6 %	8 %
Nitrogen	5 %	3 %
Hydrogen	1.3 %	1.5 %

Preprints (www.preprints.org) | NOT PEER-REVIEWED | Posted: 30 March 2022 doi:10.20944/preprints202203.0392.v1

(a) Unnotched specimen

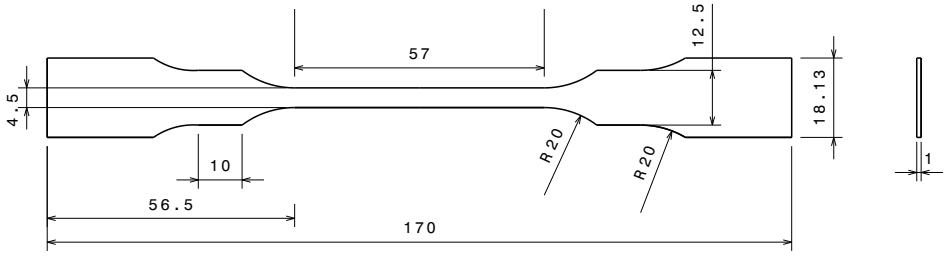

(b) Notched specimen

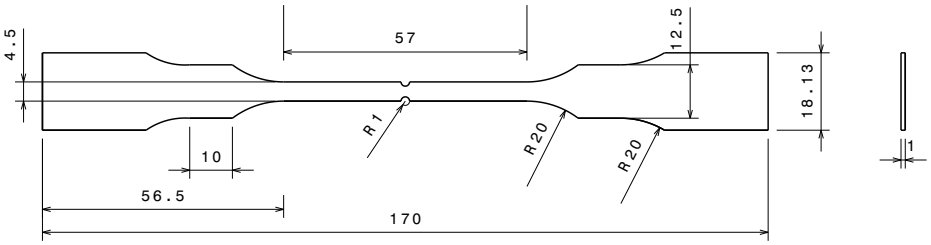

Figure 5. CAD design of tensile test specimens

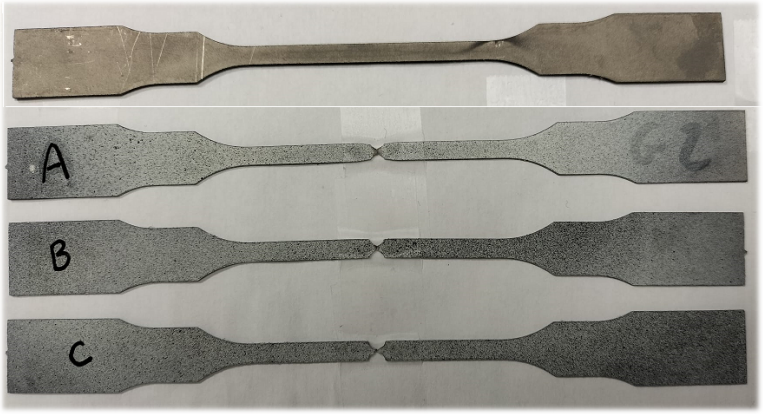

Figure 6. Notched and different unnotched specimens used in tensile tests

Preprints (www.preprints.org) | NOT PEER-REVIEWED | Posted: 30 March 2022 doi:10.20944/preprints202203.0392.v1

Table 2. Notch radius and gauge length of the studied material.

Material	Notch radius R (in mm)	Gauge length (in mm)
Rolling Direction	0	57
	0.5	56
	1	55
	1.5	54

Large deformations in the shaping process necessitate extrapolation. We chose two alternative models for this: Voce and Swift.

- Swift(or Krupkowski)'s model:

$$\sigma_{eq} = K(\epsilon_0 + \epsilon)^n \tag{4}$$

Where ϵ_0 and n define hardening constants. As a result, this work hardening law is tailored to the upper reaches of the cold deformation domain and can also be used for hot deformation.

The equation defines the identification of plastic anisotropy, or Lankford's coefficient:

$$r_\alpha = \frac{\varphi_w}{\varphi_{th}} \tag{5}$$

Where φ_w Logarithmic strain in the width direction φ_{th} Logarithmic strain in the direction of thickness

To calculate r_α, it must be able to calculate both the transverse plastic strain ϵ_{22} and the thickness strain ϵ_{33} induced during a uni-axial tensile test. However, determining thickness deformation can be difficult. The plastic incompressibility hypothesis is explored as a solution to this problem.

The materials used in this study are rigid-plastic and follow Hill's yield criterion (1948), which is an extension of von Mises' criterion that takes into consideration plastic anisotropy. The Hill48 parameters are presented in the equations below:

$$G = \frac{2}{1 + r_0}; \tag{6}$$

$$H = \frac{2r_0}{1 + r_0}; \tag{7}$$

$$F = \frac{H}{r_{90}}; \tag{8}$$

$$L = M = N = \frac{(r_{90} + r_0)(2r_{45} + 1)}{2r_{90}(1 + r_0)}. \tag{9}$$

The material is subjected to complex stresses during superplastic forming, which might result in defects (cracks, ruptures, etc.) within the part. Titanium, which is susceptible to cavitation [47], is prone to faults caused by ductile damage [48,49]. This is why it's worth thinking about this topic now because once it's included in numerical simulations, it'll be possible to foresee material deterioration and so avoid the occurrence of faults in the part. The damage of pure commercial grade 2 titanium exposed to conditions similar to those found during superplastic formation will be examined in this study. This paper proposes a Johnson-Cook type damage criterion.

- **Johnson-Cook failure criterion**

Preprints (www.preprints.org) | NOT PEER-REVIEWED | Posted: 30 March 2022 doi:10.20944/preprints202203.0392.v1

The Johnson-Cook criterion is a phenomenological approach. According to Johnson and Cook, the stress triaxiality ratio, strain rate, and temperature all influence the strain at break. The J-C rupture model is written like this:

$$\epsilon_f = (D_1 + D_2 exp(D_3 \frac{P_h}{\sigma_{eq}}))(1 + D_4 ln \frac{\dot{\epsilon_p}}{\dot{\epsilon_0}})(1 - D_5(\frac{T - T_a}{T_f - T_a})^m) \tag{10}$$

Where D_1 to D_5 are the constants of the damage model, P_h is the mean stress or hydrostatic pressure and σ_{eq} is the equivalent stress [50]. A cumulative damage law is used to define an element's damage, which can be written linearly as follows:

$$D = \frac{\sum_{\Delta\epsilon}}{\epsilon_f} \tag{11}$$

Where $\Delta\epsilon$ is the equivalent plastic strain increment, and ϵ_f It is the equivalent fracture strain at the current load, strain rate, and temperature circumstances. The material's resistance diminishes during deformation as a result of the appearance of the fracture, and the constitutive relationship of the stress for the evolution of the damages can be described as follows:

$$\sigma_D = (1 - D)\sigma_{eq} \tag{12}$$

σ_D is the damaged stress state, and D is the damage parameter, $(0 \leq D < 1)$, in equation (11). Furthermore, the triaxiality of the stresses [51–54], and the equivalent stress may be calculated from the undamaged material while accounting for plastic behavior up to the development of the necking [50].

To acquire a better result, the unnotched and notched samples were created using the waterjet cutting method in the first stage, and more than three samples were employed to obtain the flow curve. to manage the experimental inaccuracy in terms of the material's mechanical properties As shown in Figure 6, a series of experiments involving unnotched and notched flat samples were conducted simultaneously at room temperature under a variety of quasi-static strain rate conditions to investigate the effect of triaxiality of constraints on the damage behavior of grade 2 α-titanium.

For the identification of material properties as well as for the inputs of the material digital model, the flow curves acquired from the tests were divided down into elastic and plastic areas up to the necking. Furthermore, the material's mechanical properties [50] were rigorously determined through experiments, as these properties are required to precisely reproduce the material's behavior in real-world settings. Furthermore, the predicted properties were included in commercial tools, and the work hardening behavior was simulated using the isotropic work hardening model for stress triaxiality evaluation.

It is clear that the estimation of the mechanical properties of the experiments was completed flawlessly, and that it can also be used to estimate the triaxiality of the stresses without difficulty. The stress components, such as σ_1, σ_2 and σ_3, are then determined using the average of the items in the sample that fail. To determine the mean stress Ph and the equivalent stress σ_{eq}, the stress components have been swapped in equation (12).

$$\tilde{\sigma} = \frac{(\sigma_1 + \sigma_2 + \sigma_3)}{3 * \sqrt{0.5 * [(\sigma_1 - \sigma_2)^2 + (\sigma_2 - \sigma_3)^2 + (\sigma_1 - \sigma_3)^2]}} \tag{13}$$

Preprints (www.preprints.org) | NOT PEER-REVIEWED | Posted: 30 March 2022 doi:10.20944/preprints202203.0392.v1

The failure model equation can only be recast in terms of the influence of triaxiality of stresses concerning the strain of break by rearranging equation (9) by disregarding the effects of strain rate and temperature:

$$\epsilon_f = D_1 + D_2 exp(D_3 \tilde{\sigma}) \tag{14}$$

The equation (13) can be changed by substituting the stress triaxialities and the related ultimate strain values.

3.2. Forming Strategy

The proposed manufacturing method is a hybrid of two forming methods. The first is the deep-drawing method for producing conventional shapes. Deep-drawing provides for superior mechanical component characteristics while also reducing production time. It is a lengthy forming procedure. The second is the incremental forming procedure, which is used to create unique and complex shapes for the cup outline that will adhere to the bone.

The incremental sheet metal forming (ISF) technique is a viable alternative to traditional sheet metal forming processes such as hydroforming and deep drawing. It appears to be a viable response to manufacturers' desires for more flexible and cost-effective small-series and prototype solutions. For prototyping and small-batch production of complicated sheet metal, incremental forming is ideal. Due to the need for product personalization for each patient, medical implants and prostheses are one of the primary potential fields of application for the ISF process.

Forming geometric models with complex shapes, on the other hand, is still being researched. Several experimental and numerical studies have been conducted to investigate the parameters impacting this process for various metals [38,55]. The incremental forming procedure used in the suggested approach allows for the creation of a custom prosthesis for each patient, making it more comfortable and ensuring greater performance.

We'll need the cup's geometry to simulate the process. This article's method (cf. Figure 7) is based on a reverse engineering methodology. There are four steps to this method:

Step 1: A radiography of an individual pelvis. Step 2: Defining of the hip cup geometry. Step 3: The inside half of the cup is formed using a preforming process. Step 4: To manufacture the cup's outside section, an incremental forming process was used.

- Step 1 allows for the creation of a cloud of points that define the pelvic shape. This geometry is larger than the portion that has to be made.
- Step 2 tries to specify the cup's geometry before it is constructed. Escobar et al. [28,29] for a detailed description of the technique for obtaining this geometry. Initially, the fascia lunatic area is resected. The target region is fitted with a first sphere, which is positioned so that the radius is the largest without entering the bone. As a result, the approximation sphere is better fitted. Then, to produce the outside contour, a second sphere is created around the first sphere. The inner component is made by replacing the part's core with a 20-mm-diameter hemisphere. The final shape of the hip cup prosthesis is a titanium part with a large diameter of 100 mm, a thickness of 1 mm, and a hemispherical region of 20 mm in the middle area, with a wall angle of 70° to 75° in the outer zone (cf. Figure 8).
- During step 3, The inner half of the cup is constructed using a preforming process. In the middle of the hip cup, a standardized geometry is defined. This procedure is perfectly suited to this situation.
- Step 4 The incremental forming procedure is utilized in Step 4 to build the cup's outer section. At room temperature, the titanium used to make the hip cup has poor formability. Previous research has demonstrated that forming direct parts with a wall angle larger than 40° at ambient temperature is unfeasible, according to

Preprints (www.preprints.org) | NOT PEER-REVIEWED | Posted: 30 March 2022 doi:10.20944/preprints202203.0392.v1

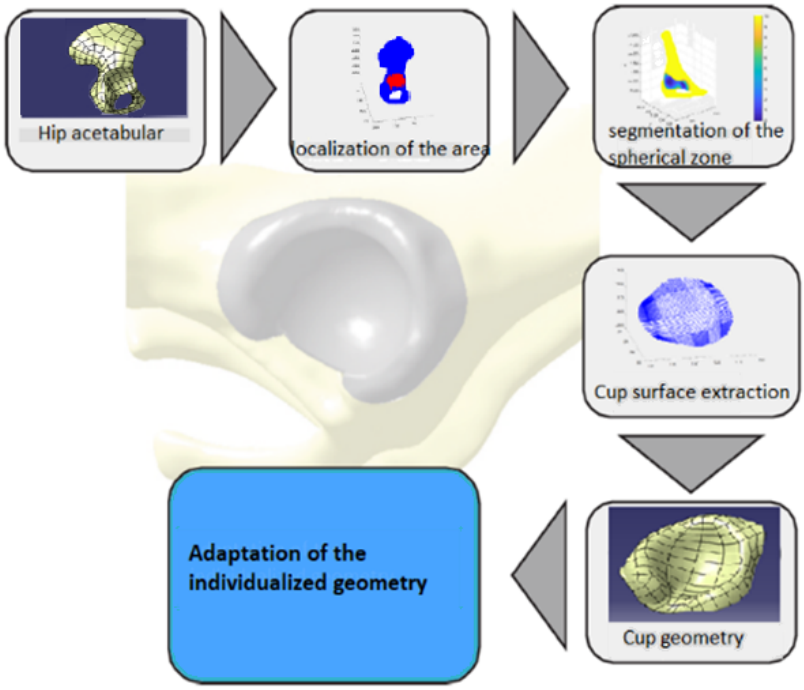

Figure 7. CAD creation of hip cup

Saidi et al. [38]. The hip cup prosthesis is intended to be formed in multiple steps by increasing the wall angle.

Formability, surface finish, thickness variation, processing time, and dimensional accuracy are all affected by the **tool path** in SPIF processes. The digital control provides the tool route (CNC). The tool follows a succession of contour lines with a vertical increment step size of $(\Delta z = 0.2mm)$ between them in a single forming step. The punch had a diameter of 2.5 mm. With a diameter of 100 mm and a thickness of 1 mm, the titanium alloy sheet was modeled in a round shape. The portion is created along the tool's trajectory, as shown in Figure 9.

We start with a triangular depiction of the cup to specify the tool's trajectory in the incremental forming phase. Indeed, the desired shape is modeled by a space mesh of triangles that define the cup's surface. We chose a spiral trajectory because of the cup's shape, and the trajectory is specified by multiple successive passages to lessen the force

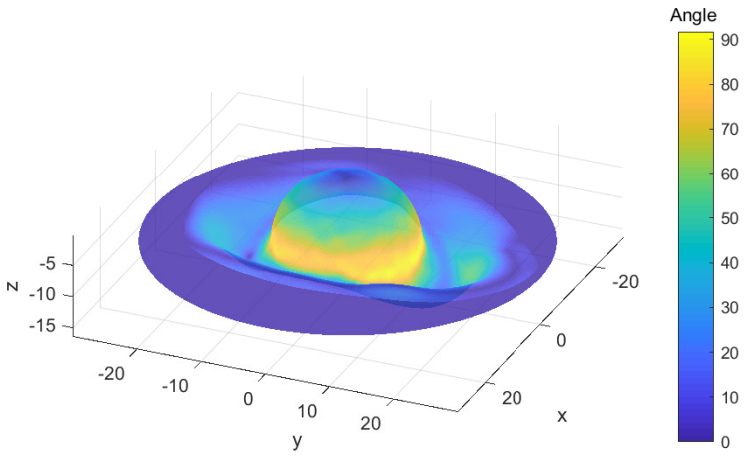

Figure 8. The analyzed part's angle variation

Preprints (www.preprints.org) | NOT PEER-REVIEWED | Posted: 30 March 2022 doi:10.20944/preprints202203.0392.v1

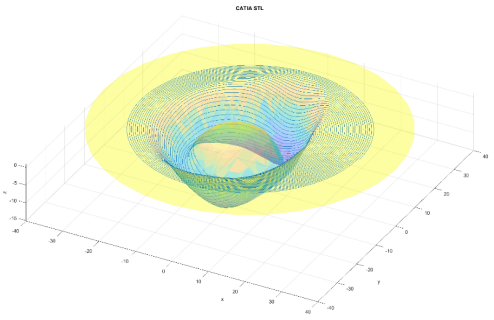

Figure 9. Tool trajectory one step

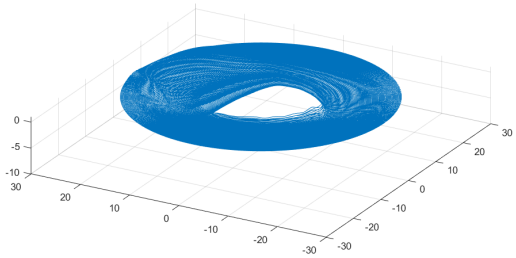

Figure 10. Tool trajectory three steps

applied to the part. The spiral follows the following equation in the horizontal plane, which is produced by the x and y axes:

$$x(t) = (R_i + (R_f - R_i)\frac{t - t_i}{t_f - t_i})cos(wt); \tag{15}$$

$$y(t) = (R_i + (R_f - R_i)\frac{t - t_i}{t_f - t_i})sin(wt). \tag{16}$$

With R_i and R_f the spiral's initial and final radii, t_i and t_f the spiral's initial and final times of passage, and ω a parameter that controls the spacing between the spiral's turns, i.e. the angular speed of rotation.

Then, for each pair $(x(t), y(t))$ on the spiral, we designate the triangle that contains the point with coordinates $(x(t), y(t), z_0)$ and we define $z(t) = z_0$. Thus, the path $(x(t), y(t), z(t))$ is defined as a tool path (cf. Figure 9).

In order to carry out several passages (cf. Figure 10), consecutive spirals are concatenated by alternating the values of R_i and R_f and by assigning progressive values to z(t):

$$z(t) = \frac{i}{N} z_0 \tag{17}$$

with N the number of total passages and i the index of the current passage $(1 \leq i \leq N)$.

3.3. Numerical simulation

- **Preforming**
  To model the stamping of the inner portion, a numerical simulation of the sheet metal stamping process is first performed. Figure 11 depicts the punch and die. They are supposed to be rigid, and rigid surfaces are used to model them.
  During this simulation, the sheet is first placed on the die by being merely subjected to gravity, then formed using the punch action, and then released. The interaction parameters between the contact zone and the sheet were defined using the Coulomb

Preprints (www.preprints.org) | NOT PEER-REVIEWED | Posted: 30 March 2022 doi:10.20944/preprints202203.0392.v1

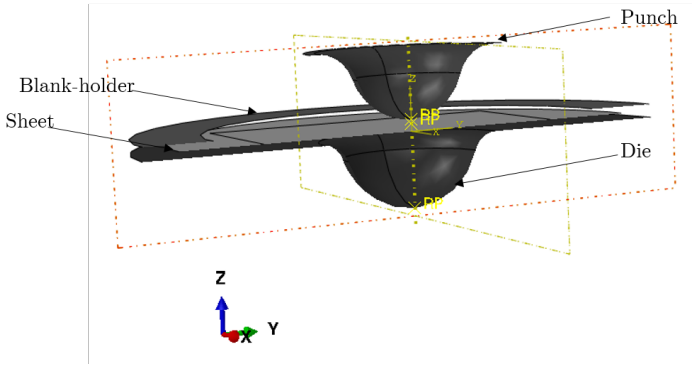

Figure 11. FE Model deep drawing

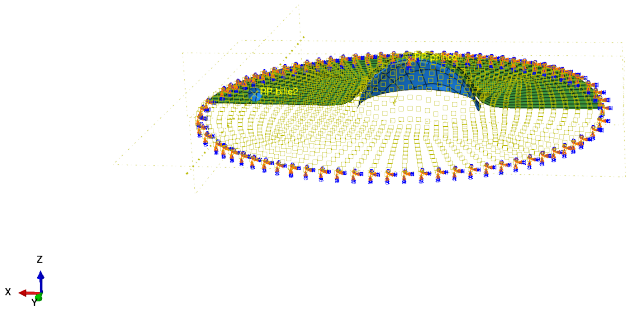

Figure 12. Exploded view of numerical model used in SPIF

friction model. The quadrilateral components with reduced integration S4R that were chosen to mesh the part were used. The sheet's mesh is made up of 37292 components.

- **Incremental forming**
  The part is created in the second stage using the tool trajectory shown in Figure 9. The forming tool follows a specified tool path to form the sheet metal in a series of incremental steps until the desired depth is reached. For incremental forming, the tools (die, blank holder, and punch) are regarded as rigid analytical surfaces. The punch is transformed into a diameter-diameter ball (dp). The die is the stationary portion on which the sheet sits, with surface-to-surface contact between the two surfaces. One of the most critical concerns for accurately simulating the incremental forming process is modeling the interaction between the tool and the sheet.
  The Coulomb's friction model, which is described as follows, defines the interaction qualities between the sheet and the contact region with the punch:

$$f = \mu N \tag{18}$$

  .
  where f is the frictional shear stress, μ is the coefficient of friction and N is the normal contact pressure.
  The punch is inflicted by displacement and the sheet is tightly secured on the blank holder.The sheet is secured tightly to the fixture and is experimentally supported on it. The sides of the initial sheet are set in all directions from a numerical standpoint, and for each simulation(cf. Figure 12).

Preprints (www.preprints.org) | NOT PEER-REVIEWED | Posted: 30 March 2022 doi:10.20944/preprints202203.0392.v1

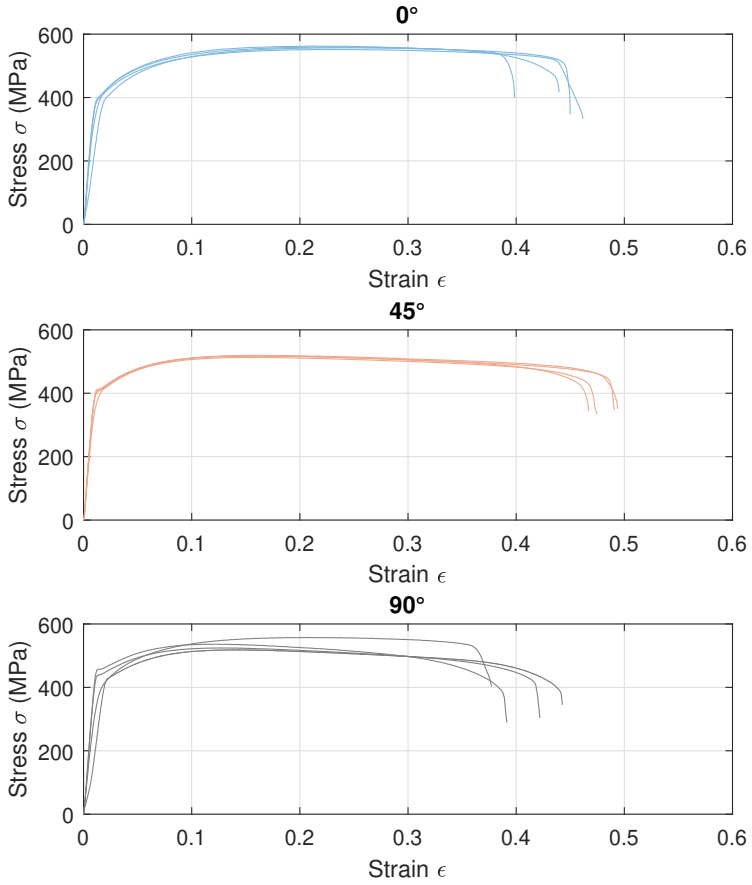

Figure 13. Conventional curve titanium grade 2

4. Results and Discussions

4.1. Experimental Results

Figure 13 shows a stress-strain curve with a clear yield point and a high ductility of the smooth specimen.

Overall, the results obtained are consistent according to the Grade 2 α-titanium abacus. We can also compare the different standard deviations (cf. Table 3) of each variable for each direction of rolling. Apart from that at 90 °, there is a high difference in the value of the tensile strength at 45 °, linked to the various uncertainties mentioned above. The superposition of flow curves in three directions is depicted in the diagram (cf. Figure 14).

Table 3. Mechanical properties of Titanium grade 2 for 3 rolling directions obtained from 4 tensile tests (mean ± standard deviation)

Rolling angle	E (GPa)	Rm (MPa)	Re (MPa)	A
0°	111.92 ± 0.29	288.50 ± 4.53	422.05 ± 5.00	32.25 % ± 1.71 %
45°	111.90 ± 0.18	288.75 ± 41.0	368.45 ± 6.29	35.90 % ± 0.84 %
90°	112.02 ± 0.17	325.25 ± 51.6	373.12 ± 5.68	35.25 % ± 2.50 %

Preprints (www.preprints.org) | NOT PEER-REVIEWED | Posted: 30 March 2022 doi:10.20944/preprints202203.0392.v1

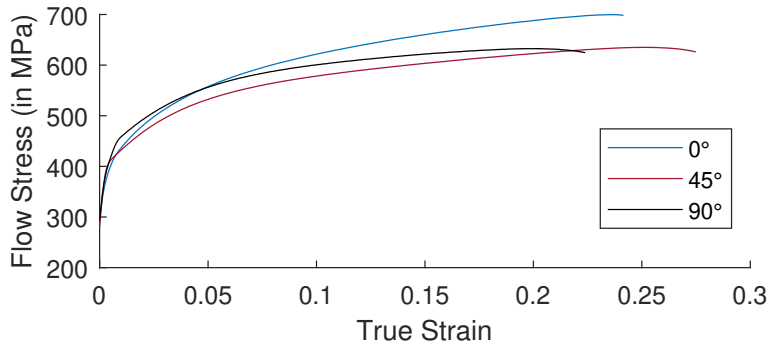

Figure 14. Flow curve titanium grade 2 for 3 directions

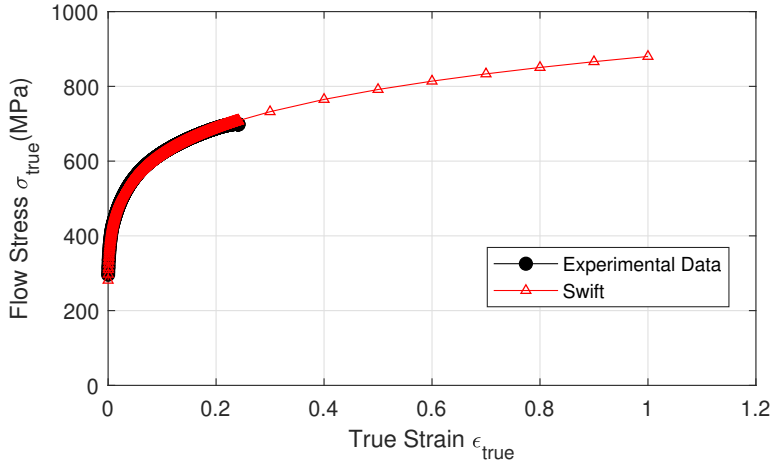

Figure 15. Comparison between experimental data and Swift model

Table 4. Swift law.

Characteristics Material	K[MPa]	ϵ_0	n
T40	**880**	**0.0578**	**0.153**

Figure 15 shows a comparison between experimental data and the Swift model. Voce's model gave an error of $1.07 * 10^{-1}$, whereas Swift's model gave an error of $8.27 * 10^{-3}$. As a result, Swift's model is employed. The values of Swift model parameters are shown in Table 4.

The change in the anisotropy coefficient during the room temperature strain hardening test for the rolling direction and a strain rate of 1 mm / min was illustrated. The plot of ϵ_{22} as a function of ϵ_{33} (obtained by considering plastic incompressibility) shows that the plastic anisotropy coefficient is not very sensitive to the level of plastic deformation. All the values of the anisotropy coefficients identified are given in Table 5. These values are in agreement with those provided by Odenberger et al.[56] for grade 2 α-titanium at the same temperature.

Table 5. Anisotropy coefficients for grade 2 α-titanium.

Orientation[°]	r
0	5.43
45	4.57
90	4.1

Preprints (www.preprints.org) | NOT PEER-REVIEWED | Posted: 30 March 2022 doi:10.20944/preprints202203.0392.v1

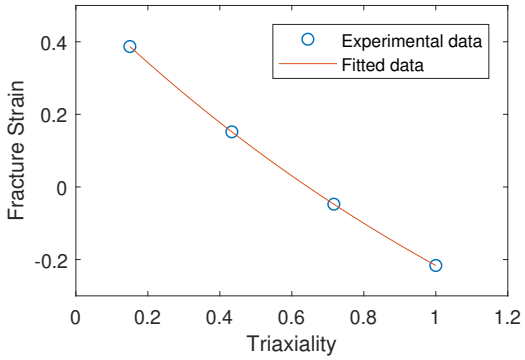

Figure 16. Fracture strain as a function of stress triaxiality

Note that the anisotropy coefficients calculated at ambient are between 4 and 5.5 (Table 5). This means that the plastic strains in the transverse direction are greater than those in the thickness. The material will therefore tend to elongate rather than thin out.

Possessing the values of the coefficients of Lankford r_0, r_{45}, r_{95}, it is possible to quickly calculate the coefficients of the anisotropic criterion of Hill48 as shown in Table 6:

Table 6. The coefficients of Hill48's anisotropic criterion for grade 2 α-titanium.

Hill48 coefficients	Values
G	0.31
H	1.68
F	0.41
L=M=N	1.83

The plot of the relation $\epsilon_f \tilde{\sigma}$ was developed from the triaxiality curve, as shown in Figure 16, the model parameters D1, D2 and D3 is calculated in Table 7.

Table 7. Johnson-Cook failure parameters for grade 2 α-titanium.

Material parameters Grade 2 α-titanium	Values
D_1	-1.157
D_2	1.685
D_3	-0.583

4.2. Numerical Results

- **Preforming**
  Figure 17 shows the visual inspection of the standardised human hip cup's generated components. At room temperature, simulating the preforming process yields satisfactory results, with a 20% reduction in blank thickness, which is a tolerable thickness. Figure 17 also depicts the homogeneous thickness distribution.
  During the forming process at room temperature, Figure 18 displays the iso-values of the scalar damage parameter described by the Stiffness Degradation SDEG. SDEG = 1.0 indicates that the appropriate elements have failed and a fracture has formed. The damage parameter SDEG is substantially lower than zero in these data, confirming the earlier result that the inner section forms at Ti = 20°C.
  We estimated the root mean square error (MSE) of the altitude z of each point on the X-Y plane to compare the theoretical and numerical profiles. The largest distance between two orthogonal locations on the surface is termed the error. As seen in Figure 19, the error was 2.38, which is small when compared to the sheet's diameter, indicating excellent conformance.

Preprints (www.preprints.org) | NOT PEER-REVIEWED | Posted: 30 March 2022 doi:10.20944/preprints202203.0392.v1

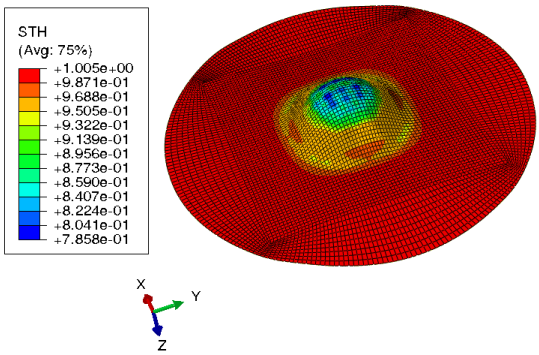

Figure 17. Distribution of shell thickness decreasing at ambient temperature: preforming process

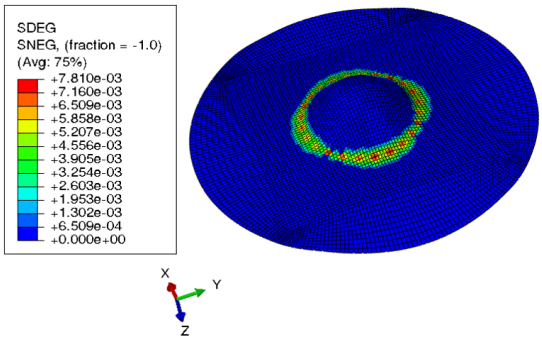

Figure 18. 3D iso-values of the Stiffness Degradation determined by Finite Elements simulation for preforming process

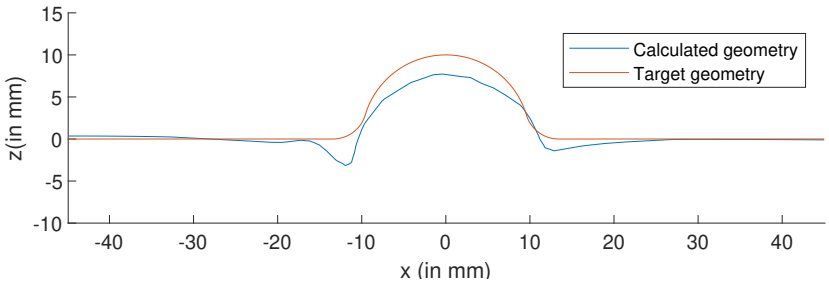

Figure 19. 2D Comparison between target and simulated geometry of the inner part

Preprints (www.preprints.org) | NOT PEER-REVIEWED | Posted: 30 March 2022 doi:10.20944/preprints202203.0392.v1

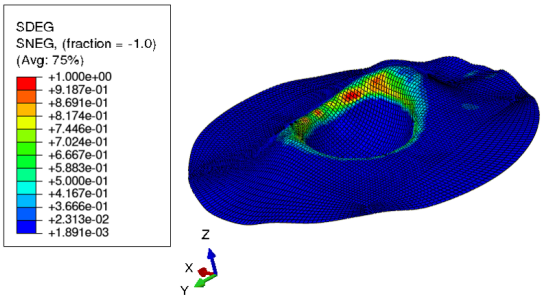

Figure 20. 3D iso-values of the Stiffness Degradation determined by Finite Elements simulation for one step forming

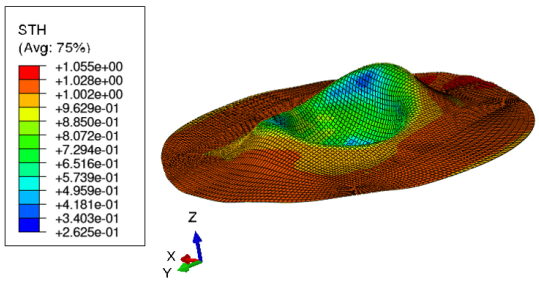

Figure 21. Distribution of shell thickness decreasing at ambient temperature: one step forming

- **Incremental forming**

4.2.1. One-step forming

Because the SDEG value in the contact zone between punch and sheet is extremely near to 1 as seen in Figure 20, the critical damage emerges at room temperature, according to these findings. The damage variable increased as predicted in these settings. These findings were given at the same time as the part's maximum deterioration at room temperature. The item is fully ruined in a short time at Ti = 20°C, as predicted, because titanium has a very poor formability at ambient temperature, as previously stated.

Figure 21 depicts the titanium blank's thickness reduction as a result of simulating the one-step incremental forming process at room temperature. According to the results of the modeling, one-step incremental forming at room temperature would result in an 80% reduction in blank thickness, which is critical and a tear. This method is difficult to finish without a cracked blank at the end due to its thinning by more than 25%, which is considered a limit to avoid the risk of cracking. It confirms the prior finding that the piece does not formed at Ti = 20°C.

4.2.2. Multi-step forming

Because the damage parameter SDEG is substantially lower than 1, Figure 22 demonstrates that the component is not harmed. According to models, multi-step incremental shaping for titanium blanks might reduce the thickness of the blank by roughly 25%. Blank thickness is improved by simulating multi-step incremental forming at the same temperature. Figure 23 shows a titanium blank and its damage parameter SDEG as a result of modeling multi-step incremental forming at room temperature.

Modeling one-step and multi-step incremental forming processes on a titaninum blank indicates that multi-step incremental forming at room temperature appears to be the most viable method for creating the prosthetic acetabulum. As a result, there is one more step to take.

Preprints (www.preprints.org) | NOT PEER-REVIEWED | Posted: 30 March 2022 doi:10.20944/preprints202203.0392.v1

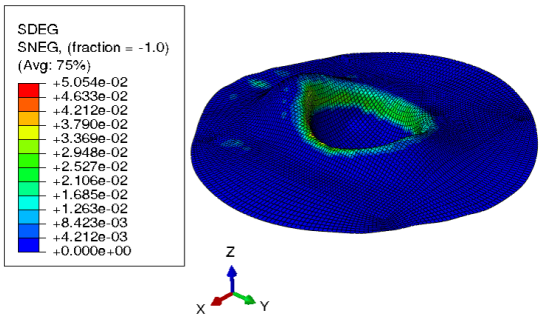

Figure 22. 3D iso-values of the Stiffness Degradation determined by Finite Elements simulation for intermediate step forming

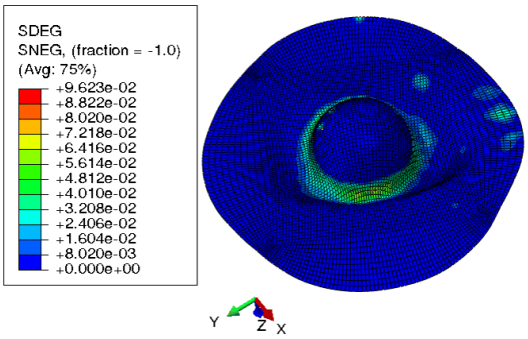

Figure 23. 3D iso-values of the Stiffness Degradation determined by Finite Elements simulation for multi-step forming

Taking the damaging effect into consideration, it was discovered that the greatest harm occurs in one-step formation. Because the plasticity of titanium is better in multi-step incremental forming operations than in single-step procedures, the ductility is substantially improved, and the yield stress is cut in half. Steps 2 to 4 should be chosen in the researched range to produce improved formability in terms of forming penetration and geometrical precision.

According to models, multi-step incremental shaping for titanium blanks might reduce the thickness of the blank by roughly 26%. Blank thickness is improved by simulating multi-step incremental forming at the same temperature. Figure 24 depicts the titanium blank and its thickness decreasing as a result of modeling multi-step incremental forming at room temperature, confirming the prior findings. This conclusion is supported by the experiences of a number of authors, including A. Bouguecha et al. [26,28,29].

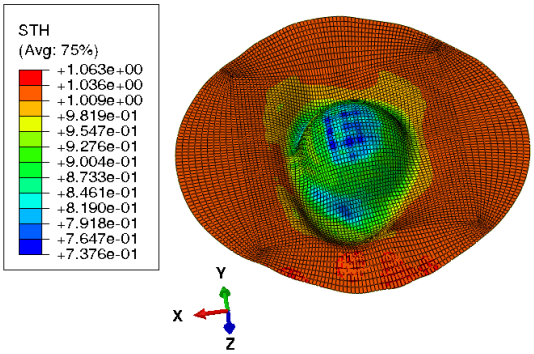

Figure 24. Distribution of shell thickness decreasing at ambient temperature: multi-step forming

Preprints (www.preprints.org) | NOT PEER-REVIEWED | Posted: 30 March 2022 doi:10.20944/preprints202203.0392.v1

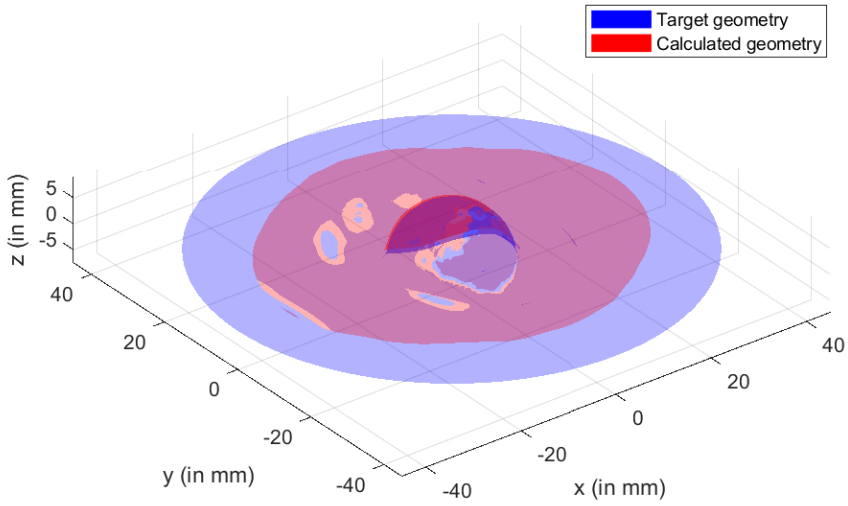

Figure 25. 3D Comparison between target and simulated geometry of hip cup prosthesis

Following that, the simulation results are compared to the specified hip cup target. For this comparison, Catia V5® (Dassault Systems, France) was used to construct the geometry of a 3D scan of the target component. The digitized geometry was compared to the simulation results to discover the best fit. In this experiment, Matlab® was used. The results of the best fit and deviation analysis are shown in the diagram. The dimensional deviation analysis (cf. Figure 25) found a minimum variation of 3.6 mm in the contour and a standard deviation of 2.52 mm across the board. As a result, the simulation and theoretical components have a high level of agreement.

5. Conclusion

The possibility of producing customized titanium hips using the ISF technique is investigated in this study by assessing FE modeling of a multi-step SPIF process for an acetabular component, and the specific difficulties and possible solutions are presented. This study's findings may be summarized as follows:

- ISF of the acetabular utilizing titanium sheets is a realistic technique that demonstrates the potential for real-world medical use.
- Multi-step manufacturing improves geometry accuracy.
- The preliminary findings are promising, and the procedure appears to be suitable for the installation of a hip prosthesis.
- To optimize these parameters for the experimental investigation, more work is needed to examine the influence of the majority of process factors on the formability of the component.

The potential of using SPIF technology to make a metal acetabular of a hip prosthesis were statistically examined in the study presented.

References

1. Ferko, M.A. Molecular Mechanisms Involved in Interleukin-1β Release by Macrophages Exposed to Metal Ions from Implantable Biomaterials. PhD thesis, Université d'Ottawa/University of Ottawa, 2018.

2. Erivan, R.; Villatte, G.; Dartus, J.; Reina, N.; Descamps, S.; Boisgard, S. Progression and projection for hip surgery in France, 2008-2070: epidemiologic study with trend and projection analysis. *Orthopaedics & Traumatology: Surgery & Research* **2019**, *105*, 1227–1235.
3. Heckmann, N.; Ihn, H.; Stefl, M.; Etkin, C.D.; Springer, B.D.; Berry, D.J.; Lieberman, J.R. Early results from the American Joint Replacement Registry: a comparison with other national registries. *The Journal of arthroplasty* **2019**, *34*, S125–S134.
4. Ackerman, I.N.; Bohensky, M.A.; Zomer, E.; Tacey, M.; Gorelik, A.; Brand, C.A.; De Steiger, R. The projected burden of primary total knee and hip replacement for osteoarthritis in Australia to the year 2030. *BMC musculoskeletal disorders* **2019**, *20*, 1–10.
5. Jaber, S.A.; Affatato, S. An overview of in vitro mechanical and structural characterization of hip prosthesis components. *Biomaterials in Clinical Practice* **2018**, pp. 585–599.
6. Bozic, K.J.; Kurtz, S.M.; Lau, E.; Ong, K.; Chiu, V.; Vail, T.P.; Rubash, H.E.; Berry, D.J. The epidemiology of revision total knee arthroplasty in the United States. *Clinical Orthopaedics and Related Research®* **2010**, *468*, 45–51.
7. Patel, A.; Pavlou, G.; Mújica-Mota, R.; Toms, A. The epidemiology of revision total knee and hip arthroplasty in England and Wales: a comparative analysis with projections for the United States. A study using the National Joint Registry dataset. *The bone & joint journal* **2015**, *97*, 1076–1081.
8. Bedard, N.A.; Elkins, J.M.; Brown, T.S. Effect of COVID-19 on hip and knee arthroplasty surgical volume in the United States. *The Journal of arthroplasty* **2020**, *35*, S45–S48.
9. et Garth W. Hastings, J.B. Manuel des propriétés des biomatériaux. Springer US, 1998.
10. D'Antonio, J.A.; Dietrich, M. *Bioceramics and Alternative Bearings in Joint Arthroplasty: 10th Biolox Symposium. Washington DC, June 10-11, 2005. Proceedings*; Springer Science & Business Media, 2006.
11. Zhang, L.C.; Kiat, E.; Pramanik, A. A briefing on the manufacture of hip joint prostheses. Advanced Materials Research. Trans Tech Publ, 2009, Vol. 76, pp. 212–216.
12. Harrysson, O.L.; Cormier, D.R. *Direct fabrication of custom orthopedic implants using electron beam melting technology*; Vol. 9, chapter, 2006.
13. Dall'Ava, L.; Hothi, H.; Di Laura, A.; Henckel, J.; Hart, A. 3D printed acetabular cups for total hip arthroplasty: a review article. *Metals* **2019**, *9*, 729.
14. Harrysson, O.L.; Cansizoglu, O.; Marcellin-Little, D.J.; Cormier, D.R.; West II, H.A. Direct metal fabrication of titanium implants with tailored materials and mechanical properties using electron beam melting technology. *Materials Science and Engineering: C* **2008**, *28*, 366–373.
15. Heinl, P.; Rottmair, A.; Körner, C.; Singer, R.F. Cellular titanium by selective electron beam melting. *Advanced Engineering Materials* **2007**, *9*, 360–364.
16. Thundal, S. Rapid manufacturing of orthopaedic implants. *Advanced Materials & Processes* **2008**, *166*, S14–S14.
17. Syam, W.P.; Mannan, M.; Al-Ahmari, A. Rapid prototyping and rapid manufacturing in medicine and dentistry: This paper presents an overview of recent developments in the field of rapid prototyping and rapid manufacturing with special emphasis in medicine and dentistry. *Virtual and Physical Prototyping* **2011**, *6*, 79–109.
18. Cronskär, M.; Bäckström, M.; Rännar, L.E. Production of customized hip stem prostheses–a comparison between conventional machining and electron beam melting (EBM). *Rapid Prototyping Journal* **2013**.
19. DebRoy, T.; Wei, H.; Zuback, J.; Mukherjee, T.; Elmer, J.; Milewski, J.; Beese, A.M.; Wilson-Heid, A.; De, A.; Zhang, W. Additive manufacturing of metallic components–process, structure and properties. *Progress in Materials Science* **2018**, *92*, 112–224.
20. Wang, P.; Sin, W.J.; Nai, M.L.S.; Wei, J. Effects of processing parameters on surface roughness of additive manufactured Ti-6Al-4V via electron beam melting. *Materials* **2017**, *10*, 1121.
21. King, W.E.; Barth, H.D.; Castillo, V.M.; Gallegos, G.F.; Gibbs, J.W.; Hahn, D.E.; Kamath, C.; Rubenchik, A.M. Observation of keyhole-mode laser melting in laser powder-bed fusion additive manufacturing. *Journal of Materials Processing Technology* **2014**, *214*, 2915–2925.
22. Garcia-Cimbrelo, E.; Diaz-Martin, A.; Madero, R.; Munuera, L. Loosening of the cup after low-friction arthroplasty in patients with acetabular protrusion: the importance of the position of the cup. *The Journal of bone and joint surgery. British volume* **2000**, *82*, 108–115.
23. Laursen, M.; Nielsen, P.T.; Søballe, K. Bone remodelling around HA-coated acetabular cups. *International orthopaedics* **2007**, *31*, 199–204.

24. Stukenborg-Colsman, C.M.; von der Haar-Tran, A.; Windhagen, H.; Bouguecha, A.; Wefstaedt, P.; Lerch, M. Bone remodelling around a cementless straight THA stem: a prospective dual-energy X-ray absorptiometry study. *Hip International* **2012**, *22*, 166–171.
25. Behrens, B.A.; Weigel, N.; Escobar, S.; Stukenborg-Colsman, C.; Lerch, M.; Nolte, I.; Wefstaedt, P.; Bouguecha, A. Development, Simulation-Based Design and Metal Forming Production of Patient-Individual Hip Cups. In *Future Trends in Production Engineering*; Springer, 2013; pp. 307–314.
26. Bouguecha, A.; Elgaly, I.; Stukenborg-Colsman, C.; Lerch, M.; Nolte, I.; Wefstaedt, P.; Matthias, T.; Behrens, B.A. Numerical investigations of the strain-adaptive bone remodeling in the prosthetic pelvis. XII Mediterranean Conference on Medical and Biological Engineering and Computing 2010. Springer, 2010, pp. 562–565.
27. Lerch, M.; Weigel, N.; Windhagen, H.; Ettinger, M.; Thorey, F.; Kurtz, A.; Stukenborg-Colsman, C.; Bouguecha, A. Finite element model of a novel short stemmed total hip arthroplasty implant developed from cross sectional CT scans. *Technology and Health Care* **2013**, *21*, 493–500.
28. Behrens, B.; Escobar, S.; Niemeier, H.; Vucetic, M.; Bouguecha, A.; Lucas, K.; Nolte, I.; Wefstaedt, P.; Lerch, M.; Stukenborg-Colsman, C.; others. Design and manufacturing of a human standardised hip cup out of titanium: Konstruktion und Fertigung einer menschlichen standardisierten Hüftpfannenprothese aus Titan. *Materialwissenschaft und Werkstofftechnik* **2016**, *47*, 608–622.
29. Escobar, S.B.; Bouguecha, A.; Almohallami, A.; Niemeier, H.; Lucas, K.; Stukenborg-Colsman, C.; Nolte, I.; Wefstaedt, P.; Behrens, B.A. The Customized Artificial Hip Cup: Design and Manufacturing of an Innovative Prosthesis. In *Biomedical Technology*; Springer, 2015; pp. 55–68.
30. Murr, L. Open-cellular metal implant design and fabrication for biomechanical compatibility with bone using electron beam melting. *Journal of the mechanical behavior of biomedical materials* **2017**, *76*, 164–177.
31. Leszak, E. Apparatus and process for incremental dieless forming. Patent US3342051A1. Technical report, published 1967–09-19, 1967.
32. Jeswiet, J.; Micari, F.; Hirt, G.; Bramley, A.; Duflou, J.; Allwood, J. Asymmetric single point incremental forming of sheet metal. *CIRP annals* **2005**, *54*, 88–114.
33. Emmens, W.; van den Boogaard, A.H. An overview of stabilizing deformation mechanisms in incremental sheet forming. *Journal of Materials Processing Technology* **2009**, *209*, 3688–3695.
34. Oleksik, V.; Trzepieciński, T.; Szpunar, M.; Chodoła, Ł.; Ficek, D.; Szczęsny, I. Single-Point Incremental Forming of Titanium and Titanium Alloy Sheets. *Materials* **2021**, *14*, 6372.
35. More, K.R.; Sisodia, V.; Kumar, S. A Brief Review on Formability, Wall Thickness Distribution and Surface Roughness of Formed Part in Incremental Sheet Forming. *Advances in Manufacturing Processes* **2021**, pp. 135–149.
36. Ziran, X.; Gao, L.; Hussain, G.; Cui, Z. The performance of flat end and hemispherical end tools in single-point incremental forming. *The International Journal of Advanced Manufacturing Technology* **2010**, *46*, 1113–1118.
37. Sabater i Armengou, M.; Garcia-Romeu, M.L.; Vives Mestres, M.; Ferrer Real, I.; Bagudanch Frigolé, I. Process parameter effects on Biocompatible thermoplastic sheets produced by incremental forming. *Materials, 2018, vol. 11, núm. 8, p. 1377* **2018**.
38. Saidi, B.; Moreau, L.G.; Mhemed, S.; Cherouat, A.; Adragna, P.A.; Nasri, R. Hot incremental forming of titanium human skull prosthesis by using cartridge heaters: a reverse engineering approach. *The International Journal of Advanced Manufacturing Technology* **2019**, *101*, 873–880.
39. Saidi, B.; Giraud Moreau, L.; Cherouat, A.; Nasri, R. Experimental and numerical study on warm single-point incremental sheet forming (WSPIF) of titanium alloy Ti–6Al–4V, using cartridge heaters. *Journal of the Brazilian Society of Mechanical Sciences and Engineering* **2020**, *42*, 1–15.
40. Saidi, B.; Giraud Moreau, L.; Cherouat, A.; Nasri, R. Accuracy and Sheet Thinning Improvement of Deep Titanium Alloy Part with Warm Incremental Sheet-Forming Process. *Journal of Manufacturing and Materials Processing* **2021**, *5*, 122.
41. Behera, A.K.; de Sousa, R.A.; Ingarao, G.; Oleksik, V. Single point incremental forming: An assessment of the progress and technology trends from 2005 to 2015. *Journal of Manufacturing Processes* **2017**, *27*, 37–62.
42. Kitazawa, K.; Nakajima, A. Cylindrical stretch-expanding of sheet metal by CNC incremental forming process. *Trans Jpn Soc Mech Eng C* **1996**, *62*, 2018–24.

43. Hirt, G.; Ames, J.; Bambach, M.; Kopp, R. Forming strategies and process modelling for CNC incremental sheet forming. *CIRP Annals* **2004**, *53*, 203–206.
44. Shamsari, M.; Mirnia, M.J.; Elyasi, M.; Baseri, H. Formability improvement in single point incremental forming of truncated cone using a two-stage hybrid deformation strategy. *The International Journal of Advanced Manufacturing Technology* **2018**, *94*, 2357–2368.
45. Malhotra, R.; Bhattacharya, A.; Kumar, A.; Reddy, N.; Cao, J. A new methodology for multi-pass single point incremental forming with mixed toolpaths. *CIRP annals* **2011**, *60*, 323–326.
46. Banabic, D. *Sheet metal forming processes: constitutive modelling and numerical simulation*; Springer Science & Business Media, 2010.
47. Nieh, T.; Wang, J.; Hsiung, L.; Wadsworth, J.; Sikka, V. Low temperature superplasticity in a TiAl alloy with a metastable microstructure. *Scripta materialia* **1997**, *37*.
48. Lemaitre, J. How to use damage mechanics. *Nuclear engineering and design* **1984**, *80*, 233–245.
49. Lemaitre, J. A three-dimensional ductile damage model applied to deep-drawing forming limits. In *Mechanical Behaviour of Materials*; Elsevier, 1984; pp. 1047–1053.
50. Murugesan, M.; Jung, D.W. Johnson Cook material and failure model parameters estimation of AISI-1045 medium carbon steel for metal forming applications. *Materials* **2019**, *12*, 609.
51. Mirone, G.; Corallo, D. A local viewpoint for evaluating the influence of stress triaxiality and Lode angle on ductile failure and hardening. *International Journal of Plasticity* **2010**, *26*, 348–371.
52. Cao, T.S.; Gachet, J.M.; Montmitonnet, P.; Bouchard, P.O. A Lode-dependent enhanced Lemaitre model for ductile fracture prediction at low stress triaxiality. *Engineering Fracture Mechanics* **2014**, *124*, 80–96.
53. Cao, T.S.; Maire, E.; Verdu, C.; Bobadilla, C.; Lasne, P.; Montmitonnet, P.; Bouchard, P.O. Characterization of ductile damage for a high carbon steel using 3D X-ray micro-tomography and mechanical tests–Application to the identification of a shear modified GTN model. *Computational Materials Science* **2014**, *84*, 175–187.
54. Bao, Y.; Wierzbicki, T. On the cut-off value of negative triaxiality for fracture. *Engineering fracture mechanics* **2005**, *72*, 1049–1069.
55. Saidi, B.; Giraud-Moreau, L.; Cherouat, A.; Nasri, R. Experimental and numerical study on optimization of the single point incremental forming of AINSI 304L stainless steel sheet. Journal of Physics: Conference Series. IOP Publishing, 2017, Vol. 896, p. 012039.
56. Odenberger, E.L.; Hertzman, J.; Thilderkvist, P.; Merklein, M.; Kuppert, A.; Stöhr, T.; Lechler, J.; Oldenburg, M. Thermo-mechanical sheet metal forming of aero engine components in Ti-6Al-4V–PART 1: Material characterisation. *International journal of material forming* **2013**, *6*, 391–402.